SAND2023-04073C

Proceedings of the 20th International Symposium on the Packaging and Transportation of Radioactive Materials

11-15 June 2023, Juan-les-Pins, France

DESIGN OF A LIGHT-WEIGHT DRAG ENHANCER TO LIMIT TERMINAL VELOCITY OF A LARGE AIR TRANSPORT CONTAINER

Kevin M. Schmidt
Sandia National Laboratories,[1] NM, USA

Sal Rodriguez
Sandia National Laboratories,[1] NM, USA

Douglas J. Ammerman
Sandia National Laboratories,[1] NM, USA

ABSTRACT

The air transport of radioactive materials always carries the risk of in-air accidents and the possible ejection of the containment package. In recognition of this, the U.S. regulations require an individual impact at the package's terminal velocity into an essentially unyielding target, unless the terminal velocity is less than 129 m/s. This impact is in addition to the sequential hypothetical accident series, which includes an impact at 129 m/s. For the large air transport package being designed by Sandia National Laboratories, the calculated terminal velocity without a drag enhancer is approximately 200 m/s. It is unlikely that it would be possible to assure the package remained leak-tight following an impact at this velocity. Therefore, limiting the terminal velocity of the package to ensure that it impacts the ground in a survivable state requires a drag enhancing system.

This paper will discuss the iterative process of using computational fluid dynamics (CFD) modelling and structural analysis to produce a unique design for a drag enhancer; beginning with the initial concept of a 2700 kg box, evolving into an approximately 110 kg aerodynamic aluminium wing that reduces the terminal velocity to below 129 m/s, therefore eliminating the need to perform an impact test at terminal velocity. In addition to calculating the terminal velocity, the CFD modelling provided the aerodynamic pressure loads acting on the drag enhancer that were used in the structural analyses to size the various members and connections.

INTRODUCTION

The Drag Enhancer (DE) is a rigid parachute designed to limit the terminal velocity of a free-falling Large Air Transport Container consisting of an Energy Absorber and Containment Vessel (EA/CV). The DE is an aeronautically designed and constructed canopy (wing) structure, like the wing structure of the aircraft used to transport the system. In free fall, the DE is a dynamic component in the system placing its components into tension and shear. Because the DE is part of the safety features for the package, ASME BPVC provisions are applied to this structure overall. Mandatory Section III, Appendix XIII-3200 of the Code [i] enables components to demonstrate safety via experimental analysis and this approach was taken for the DE. When using this approach, the allowed maximum load is 80% of the tested failure load.

The DE was designed as a unique, structurally rigid parachute, so it was determined that the overarching design documents would be the Federal Aviation Regulations (FAR) Title 14, *Aeronautics and Space* [ii], and the European equivalent from the European Aviation Safety Agency (EASA) which is basically the same document; both give general guidance as to what is expected, allowing the manufacturer to provide evidence to prove the viability of the structure. ASTM F2564, *Standard Specification for Design and Performance of a Light Sport Glider* [iii], and ASTM F2245, *Standard Specification for Design and Performance of a Light Sport Airplane* [iv], give guidance on overall aircraft airworthiness, again leaving the design details to the

[1] Sandia National Laboratories is a multi-mission laboratory managed and operated by National Technology & Engineering Solutions of Sandia, LLC, a wholly owned subsidiary of Honeywell International Inc., for the U.S. Department of Energy's

National Nuclear Security Administration under contract DE-NA0003525. UK Ministry of Defence © Crown owned copyright 2022/AWE.

manufacturer with the proof of structure to be demonstrated with conservative analysis or testing. Therefore, the design of the DE is based on information from E.F. Bruhn*'s Analysis and Design of Flight Vehicle Structures*. For the CFD calculations, Sierra Fuego, a Sandia developed CFD software program (ver. 4.32.1, 2014) was used to model the aerodynamic behavior of the air transport package. Fuego is a 3D, incompressible, reactive flow, massively parallel, generalized unstructured-mesh code with state-of-the-art turbulence models, as well as laminar and buoyant flow models. For the finite element analysis (FEA), SolidWorks Simulation Professional 2015 (ver. 3.0) was used.

DESIGN

The program requirements of the DE are to limit the terminal velocity of the EA/CV to a maximum of 129 m/s by use of one major assembly weighing a maximum of 227 kg that fits into the complete transport system (DE/EA/CV/Pallet), with a volume no greater than a cube with sides of 2.7 m. This requirement is to enable testing to meet 10 CFR 71.74 requirements using an impact speed no less than 129 m/s. Additionally the device needs to be removable at the airhead to allow for over the road transportation of the EA/CV to its destination.

The initial concept consisted of a square airfoil encasing the EA component with the bottom open to facilitate airflow (Figure 1). Subsequent research turned up a 1992 Sandia report "Impact Velocity Study and the Drag Enhancement Designs for a Plutonium Air Transportable Container" this led to significant design changes to enhance stability and reduce oscillations from developing during free fall while significantly reducing mass. The outer walls were removed; openings were added to the longitudinal ribs as well as a series of smaller diameter holes arranged on the outer sides of the top canopy. Figure 1 shows both concepts. During computational fluid dynamics (CFD) studies, it was discovered that increasing the height of the DE would increase the stability and the drag co-efficient, so the overall height was increased, and additional internal ribs were added to relieve stresses and material deformation on the inside pockets of the top canopy. Figure 2 shows the third and final design that is addressed in this paper.

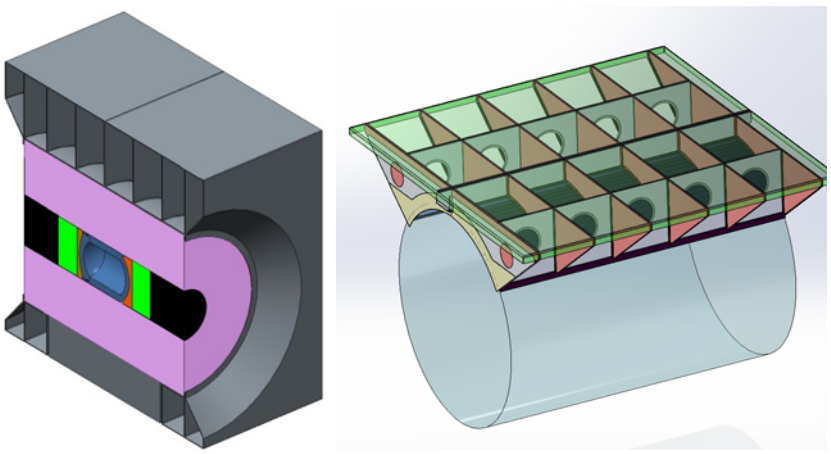

Figure 1: Left side, initial concept, complete overwrap

Right side, Ver. 2, open wing design

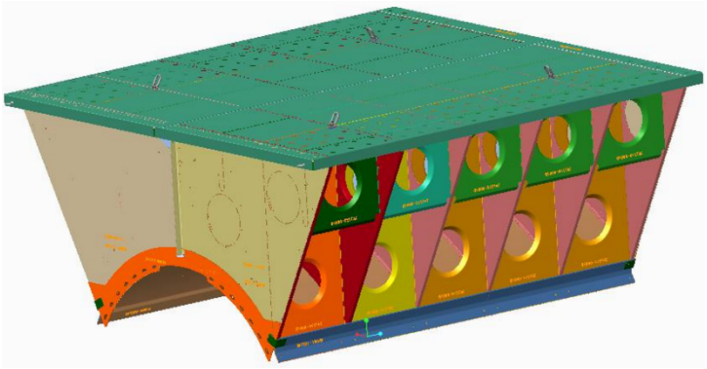

FIGURE 2: DRAG ENHANCER VER. 3, FINAL DESIGN

CFD ANALYSIS

The DE parachute design includes complex geometric features that generate a high degree of swirl. Moreover, because of the high Reynolds number (*Re*) as the DE falls through the atmosphere, it is expected to produce a vortex street that sheds eddies at a predictable frequency based on system dimensions, air properties, and velocity. As the vortices shed, this generates a transient pressure (*P*) distribution.

Prior to conducting the CFD simulations, the DE aerodynamic behavior was characterized via key dimensionless numbers and correlations to increase the fidelity of the simulations. For example, *Re* (Equation 1) determines the degree of turbulence in the flow field and fundamentally affects the aerodynamic drag coefficient, C_D. The Mach number, *Ma* (Equation 2), helps determine if the fluid is compressible or incompressible. The Knudsen number, *Kn* (Equation 3B), was used to determine if continuum fluid dynamics are appropriate. The molecular weight of the fluid, *MW* (Equation 4), determines if the fluid is Newtonian or non-Newtonian. The Strouhal number, *St* (Equations 5A and B), helps determine the vortex shedding frequency of the velocity field, and is thus a crucial parameter with respect to DE tumbling; note that Equation 5A applies to *Re* < 200,000, though its functionality reaches an asymptote value for *Re* > 50,000. The vortex field, which is also known as the von Karman vortex street, is generated by the high *Re* flow field as the DE travels through the air. The vortex shedding frequency helps assess how probable tumbling effects are. Finally, to properly apply the large eddy simulation (LES) turbulence model, the Taylor eddy size was calculated to determine how fine the mesh should be. For all fluid dynamics calculations, the air is assumed at 300 K and 101,300 Pa. The aforementioned parameters were calculated as follows:

$$(1)\ Re = \frac{x_{char} u}{\nu} = \frac{(2.5\text{m})(0.9 * 129\text{m/s})}{1.58\text{x}10^{-5}\ \text{m}^2/\text{s}} = 1.84\text{x}10^{7}\ \ (\text{very turbulent})$$

$$(2)\ \text{Mach number} = Ma = \frac{u}{u_s} = \frac{0.9 * 129\ \text{m/s}}{347.3\ \text{m/s}} = 0.33\ (\text{marginally compressive})$$

$$(3\text{A})\ \lambda_{air} = \frac{k_B T}{\sqrt{2}\pi P a^2} = \frac{\left(1.381\text{x}10^{-23}\ \frac{\text{m}^2\text{kg}}{\text{s}^2\text{K}}\right)(300\ \text{K})}{\sqrt{2}\pi\left(1.013\text{x}10^{5}\ \text{Pa}\right)\left(0.3\text{x}10^{-9}\ \text{m}\right)^2} = 1.02\text{x}10^{-7}\ \text{m}$$

$$(3\text{B})\ \text{Knudsen number} = Kn = \frac{\lambda_{air}}{x_{char}} = \frac{1.02\text{x}10^{-7}\ \text{m}}{2\ \text{m}} = 5.11\text{x}10^{-8}\ (\text{continuum domain})$$

(4) molecular weight = $MW < 5{,}000$ g/mol (Newtonian fluid [Bird, Stewart, and Lightfoot, 2000])

$$(5A)\ \text{Strouhal number} = St = \frac{fl}{u} \approx A\left(1 - \frac{B}{Re}\right) = 0.21\left(1 - \frac{19.7}{1.84\text{x}10^7}\right) = 0.21 \ \text{[Wikipedia, 2010]}$$

$$(5B)\ f = \frac{uSt}{\text{l}} = \frac{(0.9 * 129\ \text{m/s}) * 0.21}{2.5\ \text{m}} = \frac{9.75}{\text{s}} \ \text{(or } t = \frac{1}{f} = \frac{1}{9.75}\ \text{s} = \text{one vortex sheds every 0.103 s)}$$

The terminal velocity can be estimated as follows [Hoerner, 1965; Blevins, 1992],

$$(6)\ u = \left[\left(\frac{\rho_O}{\rho_a} - 1\right)\frac{2gV}{AC_D}\right]^{1/2} = \left[\left(\frac{\rho_O}{\rho_a} - 1\right)\frac{2gl}{C_D}\right]^{1/2}$$

The CFD pressure distribution results in a time-varying pressure force F_D exerted on the body's trailing surface, which can be integrated over the DE surface to estimate C_D as follows,

$$(7A)\ F_D = \text{drag force} = \frac{1}{2}\rho_a u^2 A C_D$$

$$(7B)\ C_D = 2\frac{F_D}{\rho_a u^2 A} \approx 2\frac{(A_1P_1 + A_2P_2 + \ldots A_nP_n)}{\rho_a u^2 A}$$

Finally, the LIKE algorithm [Rodriguez, 2019] was used to calculate key turbulence parameters that are useful for the CFD input and mesh models:

- turbulence intensity I_t = 0.0198
- wall friction coefficient = C_f = 0.0024
- large eddy length = ℓ_0 = 0.18 m
- Taylor eddy length = λ = 1.04x10^{-2} m
- Kolmogorov eddy length = η = 1.36x10^{-4} m
- $y(y^+=1)$ = 3.43x10^{-6} m
- turbulent kinematic viscosity = ν_t = 0.492 m^2/s
- ratio of turbulent and fluid kinematic viscosities = ν_t/ν = 3.13x10^4
- turbulence kinetic energy = k =7.89 m^2/s^2
- eddy dissipation = ε = 11.4 m^2/s^3
- eddy frequency = ω = 16.1 s^{-1}

Based on the above pre-CFD analysis, the following system-analysis physics are required: a high-*Re* turbulence model suitable for large 3D effects, including a high vortex shedding frequency and a high degree of swirl, marginally incompressible flow, continuum equations, and a Newtonian fluid [Wilcox, 2010]. Hence, the dynamic Smagorinsky LES turbulence model was selected, which is part of the Fuego CFD turbulence-model suite. Moreover, the Fuego CFD code was selected because it is suitable for modeling complex geometries under complex fluid dynamics conditions, including narrow channels, regions with strong swirl and mixing, and vortex flows. Fuego has been used successfully to model nuclear reactor fuel, plumes, jets, surface drag, flow around obstacles, subsonic compressible effects, and the lower plenum of very high temperature reactors [Fuego Theory Manual, 2016].

The DE geometry meshes consisted of 0.5-, 1.0-, 2-, 5-, 20-, and 40-million hexahedral elements. Mesh metrics were selected to minimize numerical errors, following the "gold standard" mesh metrics [Rodriguez, 2019]. In particular, the aspect ratio was set ≤ 5.0, skew was ≤ 0.5, the growth rate between adjacent computational nodes was ≤ 1.5, and the scaled Jacobian was

greater ≥ 0.5. Moreover, to ensure reasonable calculation of the shear stress, y^+ was set to 1.0 for the 20 and 40 million element meshes.

Three different configurations were modeled, as shown in Figure 3. The DE was oriented normal to the XZ plane ("standard" orientation), with the flat plate parallel to the XZ plane. Configurations with a 90° rotation about the XY and XZ planes were also conducted; see Figure 3. However, due to space limitations, only the results for the standard drop orientation are shown here.

As expected, the CFD calculations indicated that the velocity pattern became fully developed after about 3 s. Thereafter, a repetitive dynamic vortex street was generated, with large vortices shedding at a fixed frequency of about 0.1 s and a DE flow velocity in the 106.7 to 116.1 m/s range, as shown in Figure 4A. The pressure distribution is shown in Figures 4B and C. Upon applying Equations 7A and B, C_D for the standard, and the 90° clockwise rotations about the XY and XZ planes, resulted in C_D values of 1.18, 1.21, and 1.25, respectively. This indicates that the standard configuration has the flow-path of least resistance. Hence, the standard configuration provides an area superposition consisting of a primary frontal area akin to a cylinder and a secondary frontal area of the flat plate, though the ribs were mostly blocked by the large cylinder frontal area. This area superposition constitutes the rigid-parachute drag enhancer.

Note that as the vortex street eddies formed and shed, the backside velocity and pressure oscillated in time and space. It is possible that under certain conditions, the non-uniform pressure distribution can produce a time-varying load that could generate a significant rotational momentum, and thereby cause the DE to tumble. However, whereas the CFD calculations confirmed a non-uniform pressure distribution, they also indicated that the pressure did not change significantly, as shown in Figures 4B and C. The figures show that the minimum and maximum pressures were 1,500 and 7,510 Pa, respectively. The figure shows that most of the backside had a pressure distribution in the 3,500 to 7,500 Pa range, thereby indicating a mostly-uniform, small-sized pressure load, and hence, does not have a significant rotational moment. Thus, it is expected that any tendency to rotate will be quickly overcome and damped, thereby achieving a fall geometry based on the standard, self-righting fall mode configuration. Hence, the DE will seek the path of least resistance, and rather than tumble after reaching a fully-developed pattern, will free-fall in the standard configuration.

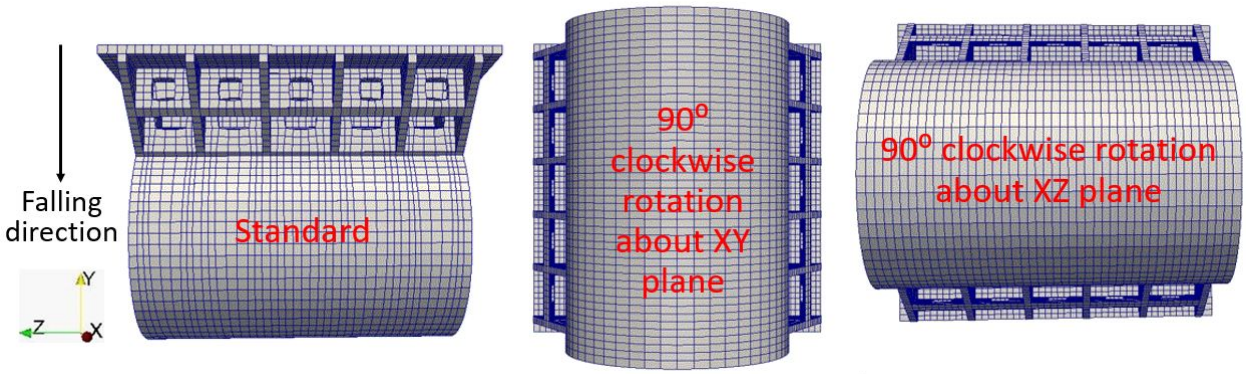

Figure 3: The three drop configurations

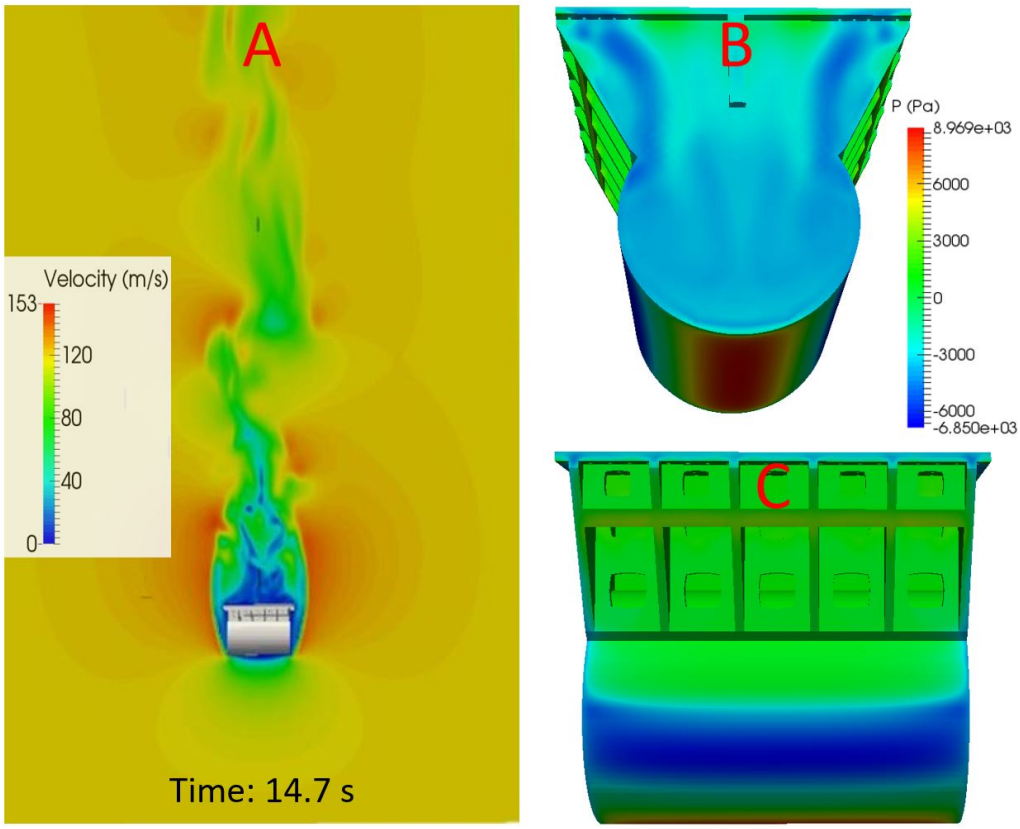

Figure 4: 4A. Vortex street flow distribution. 4B and 4C. Pressure distribution side views

STRUCTURAL ANALYSIS

The DE is essentially an open wing structure with a centre spar, ribs and webs connecting to the topskins. The end doubled ribs transfer the loads from the EA ends while the side load spreaders transfer the EA axial loads up through a series of shear webs to the topskins. The FEA tool being used for this analysis was Solidworks Simulation Professional 2015, SP 3.0. with hand calculations used to corroborate the results. Due to the complexity of the assembly, with 110 parts and 6 subassemblies, a piecewise approach was used for the analysis. All the parts are modelled as shells to reduce the number of elements. This method is ideal for thin sheet-metal parts as a nearly universal assumption for a thin case is the thickness/span ratio of the part is less than 0.05.

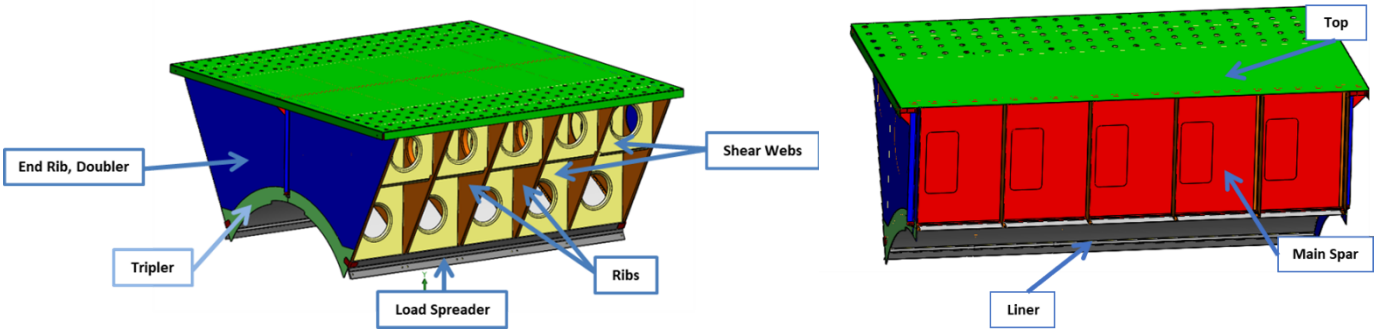

Figure 3: Structural members of the Drag Enhancer

In the CFD analysis the standard orientation (DE on top) is the most stable position (Cd =1.18) so all other orientations when falling should move towards this orientation. For this righting moment analysis, it is assumed that since the DE (113 kg) weighs so much less than the EA (4,536 kg) the center of gravity (CG) will be near the geometric center of the EA in each axis. The pressure

center of the DE is ~100.6 cm above the centerline of the EA. For this section, the pressure center is conservatively called 96.5 cm, this is used because the assumption is made that the pressure exerted on the downward face of the DE is a uniform 8.5 kPa as derived from the CFD analysis. Both end and side on orientations have righting moments of 11.98 and 9.77 kN·m respectively and will quickly come back to the standard orientation. Because this is the natural orientation of the system the rest of the analysis will be done using it.

TOPSKIN

The Topskin was cut in half along a plane coincident to the EA axis using the symmetry assumption for this drop orientation. The material applied is 2024-T3; shell elements are 0.16-cm thick. Shells are based around a surface equidistant between the two faces of the sheet metal part. The bottom face was split in a grid pattern to match the interfaces with the spar, ribs, and shear webs. The folded edges were split with faces to simulate boundary conditions imposed by various shear clips. Split lines were added to the bottom surface to simulate contact with the other components.

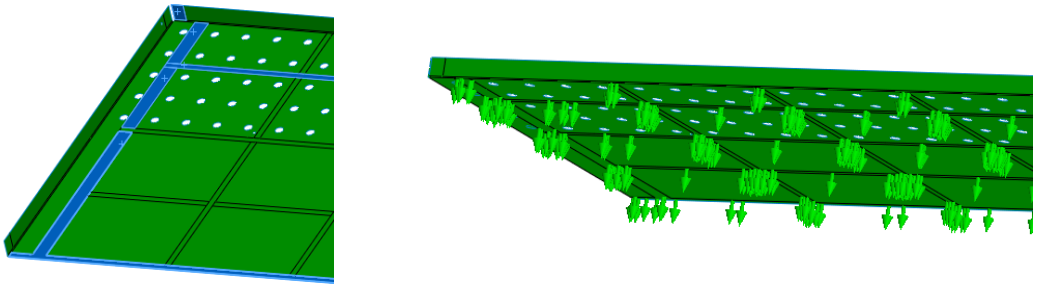

Figure 4: The left side shows the rib/doubler contact area and one shear clip contact area highlighted in blue. The right side shows the boundary conditions that were imposed on the rib/Spar/Shear Web interfaces.

Boundary Conditions

All Rib/Spar/Shear Web interfaces were restrained normal to the face and allowed their remaining degrees of freedom. A symetry condition was applied at the centreline and the shear clips were restrained normal to their mating surfaces. A pressure of 4000 Pa was applied normal to the surfaces exposed to the freestream and the shell was meshed using a curvature-based mesh, this allowed the mesher to automatically change element sizes as necessary to mesh small features such as holes and radii.

Results

Peak stresses of ~.58 MPa appear at the interface between the top and the connecting ribs over the area above the EA. This nets a factor of safety (FOS) >5.5 over yield. The max displacements (~2.16 mm) are low enough to load rib flanges in the manner they were designed. The model was then probed at the split faces representing the webs and ribs.

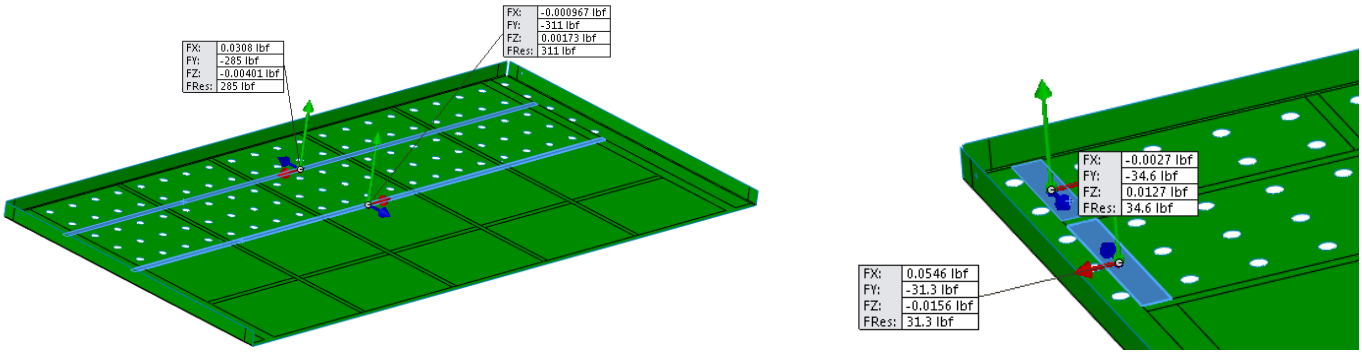

Figure 5: A couple of examples of the probe locations; left side: outer shear walls, right side end rib outer bays

INTERIOR RIBS

The Interior ribs are identical except for the direction they face and the details of attaching other components. Material applied is 2024-T3, shell elements 1.02 mm thick. Shells are based around a surface equidistant between the two faces of the sheet metal part. The mating faces were split in three places to match the interfaces with the shear webs and the top. As a method to introduce conservatism, no restoring force preventing unfolding of the flange was applied. In reality, the flange will be held in intimate contact with the top which is expected to deform only 2.16 mm at the midpoint of a 394 mm span.

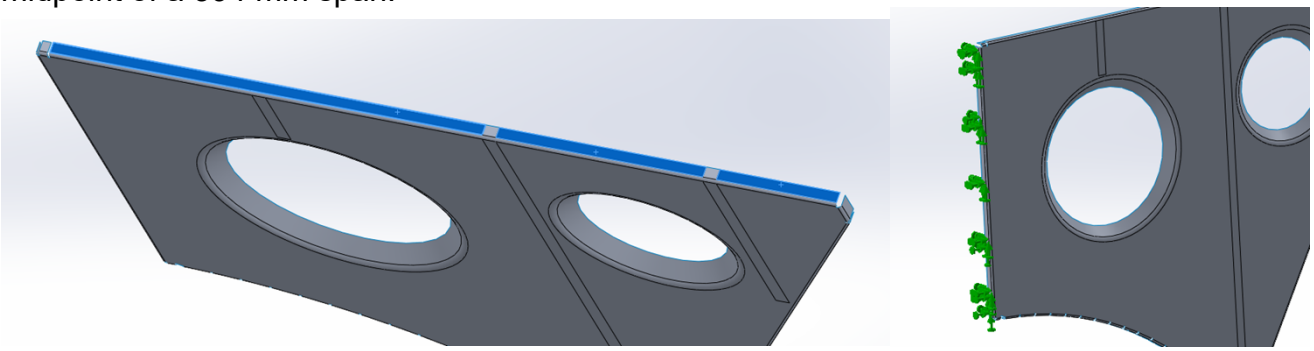

Figure 6: Left side showing the mating three split faces, right side is the interior flange that mates to the spar

Boundary Conditions

The interior flange that mates to the main spar is constrained as fixed due to the relatively high stiffness and strength of the spar. Each of the tabs that connect the bottom surface of the rib to the curved liner are only constrained along the long axis of the EA. The liner is thin and curved and will provide no real stiffness in the other two directions. The inner and outer shear web mating areas are constrained normal to the rib face. In these locations no EA loads are directly applied to the shear webs—the webs exist to attach the top and keep the ribs from buckling. The primary shear web area is constrained normal to rib surface as well as in the downward (for this orientation) direction. The shear web here attaches to the side load spreader and is a primary member for transferring EA loads to the rib and the top. The outboard end of the rib is constrained in the direction normal to the primary rib face. This is to simulate the rivet attachment to the top. As a means to introduce conservatism, no restoring force was applied to flange to prevent it from unfolding.

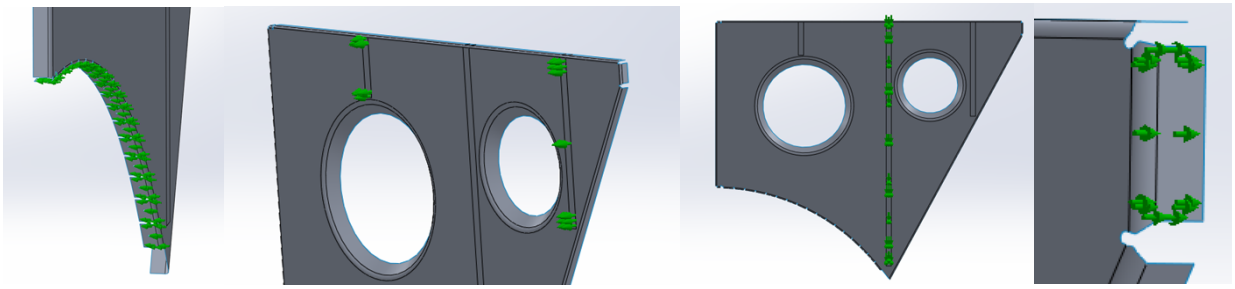

Figure 7: Left side shows lower tabs attached to liner, centre left shows the inner and outer shear webs constraints, centre right side shows the primary shear web constraints, right side shows outboard end of the rib constraint.

Consistent with reactionary forces calculated for the interior ribs during the top analysis, a force of 320 N was applied on the inboard half of the flange while the outer two flange sections had forces of 165 N applied. The shell was meshed again using a curvature based mesh.

Figure 8: Forces applied to the upper flange sections of the interior rib

Results

The analysis indicates peak stresses of 165.5 MPa at the sharp relief notches between flanges. Assuming a yield strength of 344.7 MPa, the FOS is ~2.0. The deformed plot on the left side of figure 9 shows that the primary stress and deformation is associated with the unfolding of the top flange. The right side shows the model clipped to only show stresses above 82.7 MPa. These are the tiny colored portions of the image below. This suggests a real world FOS >4.0.

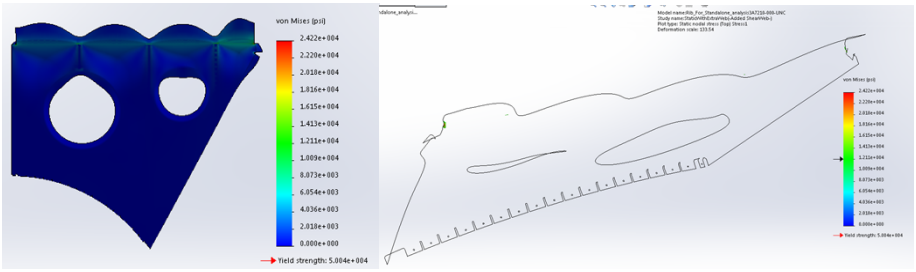

Figure 9: Deformed plot of primary stress and deformation of the flange area, scale is 133:1 right side shows the small areas subjected to stresses above 82.7 Mpa

Face deformation is greatly influenced by the flange deformation but is bounded by the unconstrained flange case. The peak face deflection between the shear webs is expected to be less than .76 mm

To better understand the effect of the relatively stiff top on the mating flanges, the boundary conditions were modified to prevent rotation of the top flange about its axis. This is a perfectly stiff boundary condition; the actual results will fall between the case above with no stiffness from the top and the case below with an infinitely stiff top. Note that peak stress is reduced dramatically with no stress concentrations due to unfolding. Applying an infinitely stiff top would increase the FOS to >25. Restraining the rotation of the top flange also dramatically reduces rib displacements.

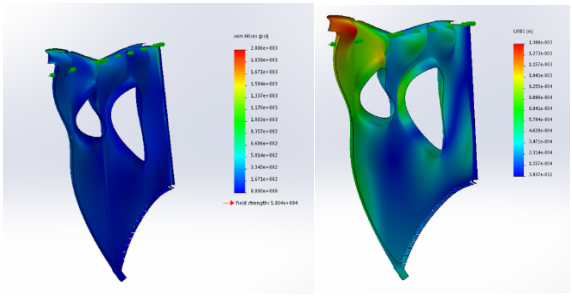

Figure 10: right side of constrained model show great reduction in peak stress, the left side shows that the greatest displacement of the face is ~.033 mm

In summary, with the most conservative boundary conditions the interior ribs show a FOS of ~2.0 at a very small volume that would self-relieve. The real world FOS in an assembly is between 4x and 20x. This is a large range, but the design has been shown to have margin.

EXTERIOR RIBS

The Exterior ribs are a laminate of an Interior rib, a rib doubler, and a rib tripler. Material for the rib and the doubler is 2024-T3, shell elements 1.02 mm thick. The tripler is 2024-T3 at a thickness of 3.2 mm. Shells are based around a surface equidistant between the two faces of the sheet metal part. The flange that mates with the top is again divided into 3 sections to align with the reaction force loads calculated from the analysis of the top.

Boundary Conditions

All mating surfaces in the assembly are treated as bonded. In practice they will be joined with numerous rivets. The rest of the constraints are the same as used in the interior rib analysis. The loads applied are also the same as the interior ribs with the addition of a pressure differential of 3 KPa applied to the inside of the primary face to simulate that pressure from the CFD analysis. Again, the shell was meshed using a curvature-based mesh.

Results

The FEA analysis indicates peak stresses of 275.8 MPa at the sharp corners of the added shear web. Assuming a yield strength of 344.7 MPa, the FOS is 1.25. Clipping the model to show only stresses above 110.3 MPa shows only tiny areas subject to higher stresses. These are the tiny, coloured portions of the image below. This suggests a real-world FOS >3.0. Due to the pressure differential across the end ribs, the deformation is a relatively large 10 mm at the largest unsupported area. Although not necessarily a problem, displacements this large can lead to nonlinear failure modes.

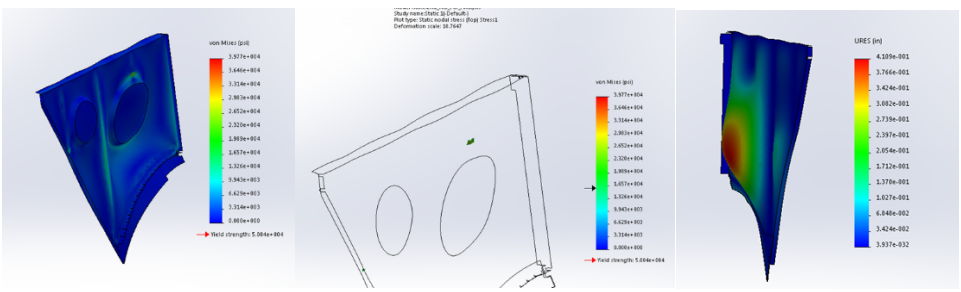

Figure 11: right side shows stresses experienced by the assembly around the larger lightening hole, centre shows the areas experiencing stresses larger than 110.3 MPa.

Right side model shows the 10 mm displacement of the panel

Based on these results the interior shear panels were elongated and the lightening holes were moved downward to stiffen the lower rib section.

PRIMARY SHEAR WEB:

The Primary Shear Webs are the primary members for transferring loads from the sides of the EA to the DE. Their bottom edge is laminated with a 0.5 mm thick liner and the 6.35 mm thick spreader bar which transfers the bolt loads to the primary shear web across its entire lower edge. That transfer of loads will be handled separately. Material for the shear web is 2024-T3, shell elements 1.02 mm thick. Shells are based around a surface equidistant between the two faces of the sheet metal part.

Boundary Conditions

The side flanges are restrained from moving normal to the face and parallel to the long edge, simulating the ribs backed up by the neighboring shear web. The bottom flange is held as fixed. This simulates the liner/shear web/ load spread bar sandwich that is designed specifically to mimic this condition and spread bolt loads to the shear web. The top flange is restrained against rotation to simulate the stiffening effect of the top.

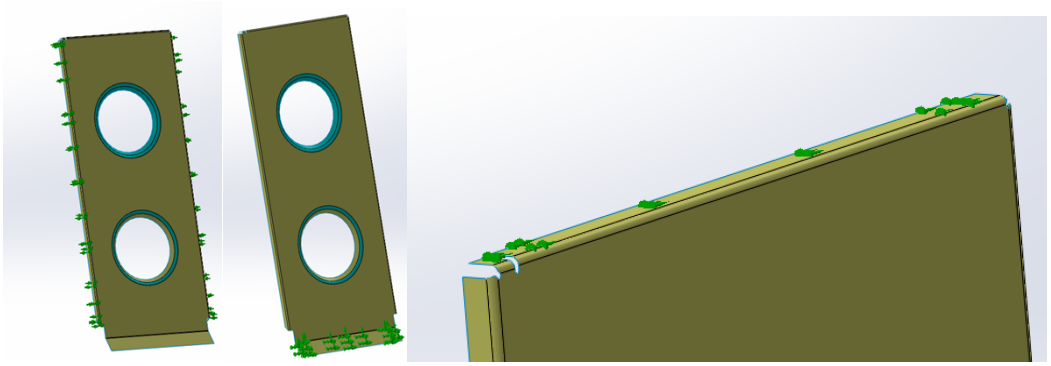

Figure 12: Left side, side flange restraints, normal and parallel to long edge, centre, bottom is held fixed, Right side, top flange restrained against rotation.

Loads

The top flange has a load of 289 N applied normal to the face representing its portion of the overall distributed shear web reaction force calculated in the analysis of the top. The side flanges have a load applied parallel to their long axis of 333.6 N each. This simulates the transfer of tension to the ribs and creates the mating boundary condition on the ribs. The Shell was meshed using a curvature based mesh.

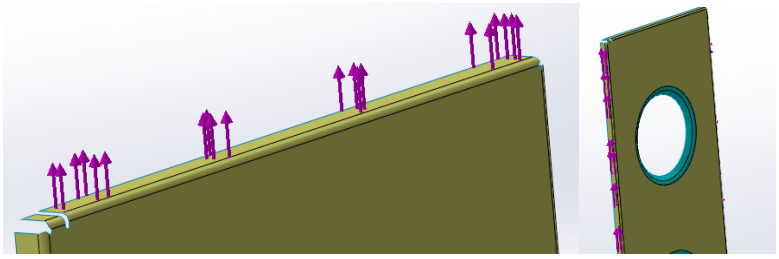

Figure 13: Left side, forces applied along the top flange. Right side, forces applied parallel to the side flanges.

Results

Stress is fairly distributed with a peak of 11.7 MPa at the upper flange. This indicates a FOS of ~29. Suppressing the boundary condition preventing rotation of the top flange yields a peak stress of 179.3 MPa. The attendant FOS is ~2 and is the worst-case assumption. Displacements are less than .076 mm in the fully constrained case while the unconstrained case shows a deflection of ~2 mm. The as built unit is expected to be closer to the fully constrained case.

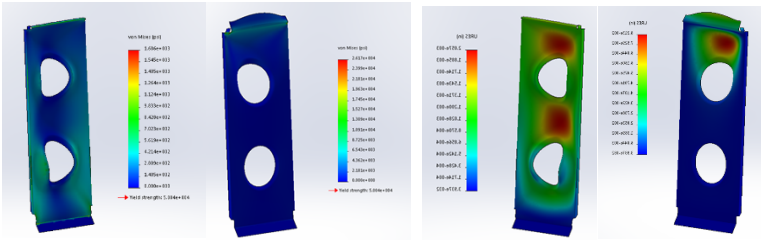

Figure 14: Left side, constrained and unconstrained stresses top flange, Right side constrained and unconstrained deflection.

MAIN SPAR

The main spar is a lamination of two identical parts. The lightening holes are asymmetric to prevent flow between the two sides of the DE. One of the parts will be analyzed using the symmetric assumption. Material for the shear web is 2024-T3, shell elements 1.6 mm thick. Shells are based around a surface equidistant between the two faces of the sheet metal part. The attach points for the interior and exterior ribs are divided by spilt lines in the shell.

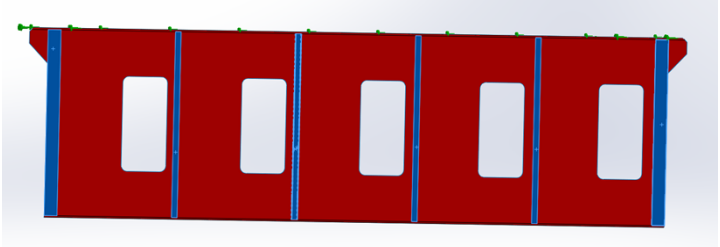

Figure 15: main spar, with split line simulating the ribs.

Boundary Conditions

The face of the spar that mates to the identical part is held as fixed to simulate the symmetry condition and the stiffness imparted by the remaining structure. The top flange is prevented from unfolding along its long axis, simulating the restraint from the overlapped top skins and the

remainder of the structure. The end rib locations are constrained normal to the top surface simulating the load transfer from the end ribs.

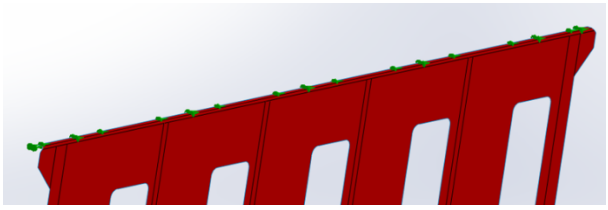

FIGURE 16: The top flange is fully constrained with the end rib locations constrained normal to the top surface.

Each end rib location is subject to a 2225 N force, these were obtained from the end rib pressure analysis. The interior ribs apply only 80 N to the spar, the majority of the rib loads are carried directly to the top-skin. These forces were found through the interior rib analysis. A force of 1348 N was applied to the top flange, in practice this would be distributed to the end ribs also, but the entire force was applied here to be conservative. A pressure of 4000 Pa was applied to the inside face.

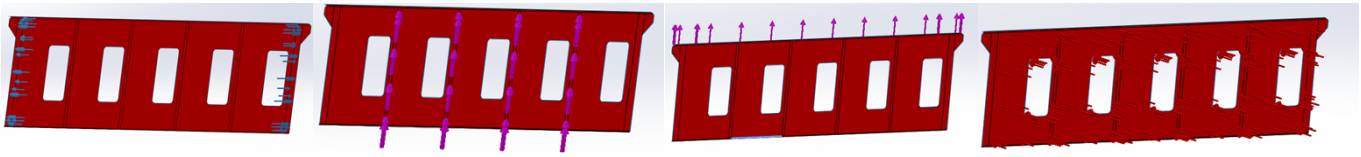

Figure 17: Forces applied to end rib locations, parallel to rib locations, normal to top flange and pressure applied to the inner face.

Results

Stress is uniformly distributed with a peak of 3.2 MPa at the upper flange. This indicates a FOS of ~108. Suppressing the boundary condition preventing rotation of the top flange yields a peak stress of 148.2 MPa. The attendant FOS is ~23 and is the worst-case assumption.

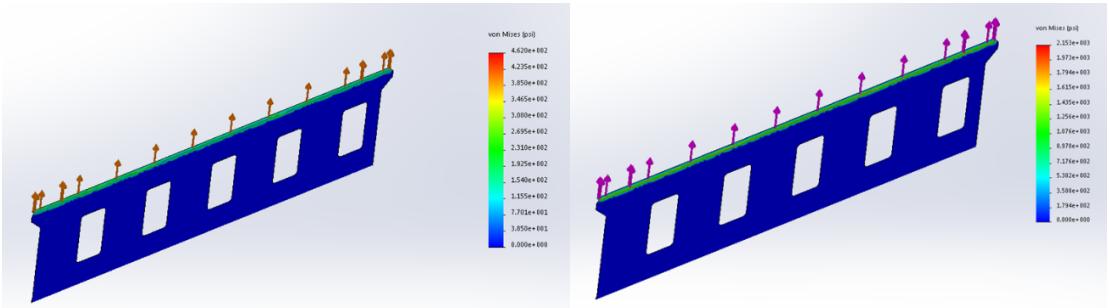

Figure 18: Left side, peak stress of constrained upper flange, right side, peak stress of unconstrained upper flange.

CONCLUSIONS

Using a combination of CFD and structural FEA, a viable, aerodynamic drag enhancer was designed through initial concept to the final design. During the process the design was reduced from a 2700 kg box to a 110 kg wing that reduces the terminal velocity to below 129 m/s, therefore eliminating the need to perform an impact test at terminal velocity. In addition to calculating the terminal velocity, the CFD modelling provided the aerodynamic pressure loads acting on the drag enhancer that were used in the structural analyses to size the various members and connections.

REFERENCES

[i]. American Society of Mechanical Engineers (ASME), Boiler & Pressure Vessel Code, Section III, *Rules for Construction of Nuclear Facility Components,* Appendices, 2017 Edition, New York, NY.

[ii]. Federal Aviation Regulations (FAR) Title 14, *Aeronautics and Space,* Part 25, subpart C – Structure.

[iii]. American Society for Testing and Material, ASTM F2564-14, *Standard Specification for Design and Performance of a Light Sport Glider,* ASTM International, 2014, West Conshohocken, PA.

[iv]. American Society for Testing and Material, ASTM F2245-16c, *Standard Specification for Design and Performance of a Light Sport Airplane*, ASTM International, 2016, West Conshohocken, PA.

Bird, R., W. Stewart, and E. Lightfoot, *Transport Phenomena*, John Wiley & Sons, 2nd Ed., 2007.

Blevins, R. D., *Applied Fluid Dynamics Handbook*, Kreiger Publishing Company, 1992.

Fuego Theory Manual, "SIERRA Low Mach Module: Fuego User Manual – Version 4.40", Sandia National Laboratories, 2016.

Hoerner, S. F., Fluid-Dynamic Drag, Hoerner Fluid Dynamics, PO Box 21992, Bakersfield Ca, Ph. (661) 665-1065, 1992.

Rodriguez, S., *Applied Computational Fluid Dynamics and Turbulence Modeling: Practical Tools, Tips and Techniques*, Springer Int. Pub., DOI: 10.1007/978-3-030-28691-0, www.cfdturbulence.com, 2019.

Wilcox, D. C., *Turbulence Modeling for CFD*, 3rd Ed., 2010.